

Article

# Comparative Study on Rosseland's Heat Flux on Three-Dimensional MHD Stagnation-Point Multiple Slip Flow of Ternary Hybrid Nanofluid over a Stretchable Rotating Disk

Gaurav Gupta and Puneet Rana \*

School of Mathematical Sciences, College of Science and Technology, Wenzhou-Kean University, Wenzhou 325060, China

\* Correspondence: puneetranaiitr@gmail.com or prana@kean.edu; Tel.: +91-9711333514

**Abstract:** This article investigates the three-dimensional magneto stagnation-point flow of ternary hybrid nanofluid caused by a radially extended infinite gyrating disk with multiple slip effects. The main concern is to analyze the characteristics of heat transport when linear thermal radiation (LTR), quadratic thermal radiation (QTR), and full nonlinear thermal radiation (FNTR) are significant. Ternary fluid is a composition of water, spherical-shaped silver, cylindrical-shaped aluminum oxide, and platelet-shaped aluminum nanoparticles. Non-uniform heat source effects are taken into account. The governing equations are constructed using a single-phase nanofluid model using boundary layer theory and von Karman variables. The consequent nonlinear problem is solved with an efficient finite element method and the results are verified with the available data. The Nusselt number and friction factors are computed for both clean fluid and ternary nanofluid subjected to three different forms of Rosseland's thermal radiation. Our results demonstrate that the rate of heat transport (Nusselt number) is higher in the FNTR case than in QTR and LTR, and it is even higher for ternary nanofluid compared to clean fluid. Further, the heat transport rate gets reduced for a higher heat source parameter. The rotation of the disk escalates the shear stress along both the radial and axial directions. The multiple slip boundary conditions lead to condensed boundary layers over a disk surface.

**Keywords:** rotating disk; stagnation flow; radial stretching; ternary hybrid nanofluid; thermal radiation; finite element method

**MSC:** 76M10; 76U05; 80A19; 80A21



**Citation:** Gupta, G.; Rana, P. Comparative Study on Rosseland's Heat Flux on Three-Dimensional MHD Stagnation-Point Multiple Slip Flow of Ternary Hybrid Nanofluid over a Stretchable Rotating Disk. *Mathematics* **2022**, *10*, 3342. <https://doi.org/10.3390/math10183342>

Academic Editors: Katta Ramesh and Rama Subba Reddy Gorla

Received: 12 August 2022

Accepted: 9 September 2022

Published: 15 September 2022

**Publisher's Note:** MDPI stays neutral with regard to jurisdictional claims in published maps and institutional affiliations.



**Copyright:** © 2022 by the authors. Licensee MDPI, Basel, Switzerland. This article is an open access article distributed under the terms and conditions of the Creative Commons Attribution (CC BY) license (<https://creativecommons.org/licenses/by/4.0/>).

## 1. Introduction

Recently, the role of nanofluids has substantially originated in various applications due to their properties being incomparably superior to those of other working fluids. The variety of nanoparticles is immersed in the working fluids to synthesize the nanofluids, and thus the optical, magnetic, thermal, mechanical, and electrical characteristics have been improved. Its relevance is found in microreactors, solar collectors, microchannel heat sinks, enzymatic biosensors, bioseparation systems, and micro-heat tubes. For extended applications, readers are referred to Das et al. [1], Saidur et al. [2], and Yu and Xie [3]. The idea behind the inclusion of a single type of nanoparticle in a working fluid is to improvise thermal, rheological, or chemical properties. However, some applications require improvements in various characteristics of the working fluids. Therefore, the inclusion of multiple types of nanoparticles of the same volume improves the general characteristics of the working fluids; the resulting fluid is called a hybrid or composite nanofluid [4]. For example, aluminum oxide ( $Al_2O_3$ ) exhibits superior chemical properties, while copper ( $Cu$ ), alumina ( $Al$ ), and silver ( $Ag$ ) possess better thermal characteristics, thanks to the inclusion of  $Al_2O_3$  and  $Al$  in the working fluid (say  $H_2O$ ), which not only improve both characteristics of  $H_2O$ , but also make it more stable and capable [5]. Furthermore, the use of

various nanoparticles in various forms serves the purpose even more effectively. Therefore, in this study, we considered a ternary composite nanofluid formed by *Al* nanoparticles in spherical form,  $Al_2O_3$  in cylindrical form and *Ag* in the form of platelets and water ( $H_2O$ ). Elnaqeeb et al. [6] used copper nanotubes,  $Al_2O_3$ , and graphene nanoparticles in water to form a ternary nanofluid in the investigation of the suction/injection process in the 3D dynamics caused by dual stretching of the plate. Animasaun et al. [7] considered  $Al_2O_3$ , *Al* and *Ag* nanoparticles to examine the induced magnetism at the stagnation point dynamics on a convectively heated plate. Shah et al. [8] utilized  $Cu - Al_2O_3 - Ag - H_2O$  fluid to investigate the thermodynamics of second-grade liquid using the Atangana–Baleanu approach. Recently, several researchers [9–13] examined the thermal features of ternary fluid.

The fluid dynamics caused by the rotation of the disk surface were first studied by von Karman [14], and he became familiar with a set of variables (known as the von Karman variables) to solve the problem in a self-similar way. Stagnant point flows in blunt rotating bodies are substantial in several applications [15] and crucial for understanding heat/mass transport since the stagnation-point region contains the greatest heat/mass transport and pressure [15]. White [16] and Jensen et al. [17] highlighted applications such as the cooling of silicon wafers, rotary blades, and chemical steam processes. Turkyilmazoglu [18] studied 3D dynamics in the stagnation-point region beyond a rotating disk with a vertical magnetic field and showed that vertical magnetism thickens the flow layer in the disk. Mustafa et al. [19] extended their work [18] to heat transport and ferrofluid using the finite difference scheme. They reported that the rate of heat transport at the stagnation point was improved due to the suspension of ferrous particles. Prabhakar et al. [20] examined the dynamics of the Casson fluid at the stagnation point and the convective heat condition created by the enlargement of the disk surface. Ahmed et al. [21] scrutinized the time-dependent dynamics of Maxwell fluid-carrying nanoparticles due to the extension disk and the Joule dissipating. They reported that Joule dissipation greatly increases the thermal distribution, and the chemical reaction depresses the distribution of the solute. Hafeez et al. [22] used the Midrich technique to study the dynamics of the Oldroyd-B nanofluid in a stagnation point created by the extended disk surface and found that thermal radiation significantly increases thermal distribution. Recently, Ahmad and Nadeem [23] used MWCNT- $H_2O$ - $C_2H_2F_4$  and SWCNT- $H_2O$ - $C_2H_2F_4$  to study the stagnation-point dynamics due to the extension of the disk surface. In this direction, several researchers [24–27] examined the disk flow problems. However, the stagnation-point dynamics of the ternary composite fluid on a traction disk have not yet been studied. Therefore, we intend to examine the stagnation-point dynamics on an enlarging disk utilizing  $H_2O - Al_2O_3 - Al - Ag$ .

On the other hand, heat transport with the appearance of thermal radiation finds applications in nuclear power plants, solar systems, astrophysical flows, gas production, spacecraft, electricity generation, etc. Rosseland [28] proposed the model to examine thermal radiation for gray and coarse media, and it has been widely used. The linearized form of the Rosseland radiative heat flux was incorporated by Viskanta and Grosh [29], Perdakis and Raptis [30], and Cortell [31] to study boundary layer heat transport with the hypothesis of a small thermal difference in the system. Pantokratoras [32] considered a large temperature difference in the system and studied the Rosseland radiation without any simplification, and it is known as full nonlinear thermal radiation (FNTR). Recently, Mahanthesh [33] considered the quadratic form of the Rosseland radiation. Subsequently, Thriveni and Mahanthesh [34] investigated the effects of quadratic thermal radiation (QTR) on a mixed quadratic convective transport of hybrid nanofluids and determined that QTR improves heat transport of the fluid system. The effects of QTR are examined by Shaw et al. [35] to study the magneto heat transfer characteristics in nanofluids, Purna Chandra et al. [36] to study the heat transport in the Ree–Eyring fluid and Rana et al. [37] to study heat transport in MWCNT-MgO/EG.

However, there are no concrete studies available to compare the three different forms of Rosseland thermal radiation on the flow and heat transport on a disk surface. The novelty of

the present study was to perform a comparative study of three different forms of Rosseland thermal radiation on a ternary nanofluid. Therefore, we performed a comparative thermal analysis subjected to the three different forms of Rosseland thermal radiation (namely, linear thermal radiation (LTR), quadratic thermal radiation (QTR), and full nonlinear thermal radiation (FNTR)) on the stagnation-point magneto-dynamics of  $H_2O - Al_2O_3 - Al - Ag$  ternary nanofluid on an extended disk with multiple slip effects. This study is not yet reported in the literature. The mathematical formulation is carried out by using conservation laws of mass, flow, and heat transport and simplifying them by applying von Karman variables. The consequent nonlinear problem is solved by an efficient finite element method [38–41]. We provide the Nusselt number and fraction factor data for both clean fluid and ternary nanofluid subjected to three different forms of Rosseland thermal radiation.

### 2. Formulation of the Problem

Stagnation-point three-dimensional laminar dynamics of ternary composite nanofluid induced by spinning and extending the disk and free-stream velocity are considered. Ternary fluid is flowing over a stretchable disk surface, it is a hydraulically open system, and flow occurs due to the free-stream velocity and stretching of the disk surface. The testing fluid is water ( $H_2O$ ) conveying cylindrical aluminum oxide ( $Al_2O_3$ ), spherical aluminum ( $Al$ ), and platelet silver ( $Ag$ ) nanoparticles (NPs). A single-phase nanofluid model is used. The single-phase nanofluid model treats the nanoparticle suspension as a single liquid rather than a multiphase fluid due to the small volume fraction of nanoparticles. It also includes the effective thermophysical properties of the nanofluid. Therefore, we have employed the single-phase nanofluid. Considering the magnetic field perpendicular to the disk, the induced magnetic field is mistreated. The viscous dissipation and Joule dissipation effects are ignored. The base fluid properties are assumed to be constant. The Rosseland radiative flux and non-uniform heat sources are accounted for, thus the governing equations for incompressible ternary nanofluid become (see [18,19]):

Continuity Equation:

$$\nabla \cdot \vec{U} = 0 \tag{1}$$

Momentum Equation:

$$\rho_{tnl} \left( \frac{\partial \vec{U}}{\partial t} + (\vec{U} \cdot \nabla) \vec{U} \right) = -\nabla p + \mu_{tnl} \nabla^2 \vec{U} + \vec{J} \times \vec{B} \tag{2}$$

Energy Equation:

$$(\rho C_p)_{tnl} \left( \frac{\partial T}{\partial t} + (\vec{U} \cdot \nabla) T \right) = k_{tnl} \nabla^2 T - \nabla q_r + q''' \tag{3}$$

The radiative heat flux  $q_r$  (see [28–30]):

$$q_r = -\frac{4\sigma^*}{3k^*} \nabla T^4 \tag{4}$$

The non-uniform heat source  $q'''$  (see [42,43]):

$$q''' = Q_t(T - T_\infty) + Q_e(T_w - T_\infty) \exp\left(-\frac{nz}{r} \sqrt{Re}\right) \tag{5}$$

Operators in the cylindrical system are

$$(\nabla, \nabla^2) = \left( \frac{\partial}{\partial r} \hat{e}_r + \frac{1}{r} \frac{\partial}{\partial \varphi} \hat{e}_\varphi + \frac{\partial}{\partial z} \hat{e}_z, \frac{\partial^2}{\partial r^2} + \frac{1}{r} \frac{\partial}{\partial r} + \frac{1}{r^2} \frac{\partial^2}{\partial \varphi^2} + \frac{\partial^2}{\partial z^2} \right) \tag{6}$$

where  $t$  is the time,  $(\hat{e}_r, \hat{e}_\varphi, \hat{e}_z)$  unit vectors along  $(r, \varphi, z)$  cylindrical co-ordinates,  $\vec{U}$  is the velocity vector,  $\vec{J}$  is the current density,  $\vec{B}$  is the magnetic field,  $p$  is the pressure,  $T$  is the temperature,  $\rho C_p$  is the specific heat,  $k^*$  is the Rosseland mean absorption,  $\sigma^*$  is the Stefan–Boltzmann constant,  $Q_t$  is the temperature-dependent source coefficient,  $n$  is the nonnegative constant,  $Q_e$  is the exponential-space-dependent coefficient,  $Re$  is the Reynolds number, and subscripts  $tnl, w$  and  $\infty$  denote the ternary nanoliquid, wall of the disk, and ambient state, respectively.

Figure 1 depicts that the disk rotates with an angular velocity  $\Omega$  in the  $z$ -direction. The disk is extended axially with a velocity  $u_w = cr$ , where  $c > 0$ . The system has a free-stream velocity  $u_e = ar$ , where  $a > 0$  and free-stream temperature  $T_\infty$ .

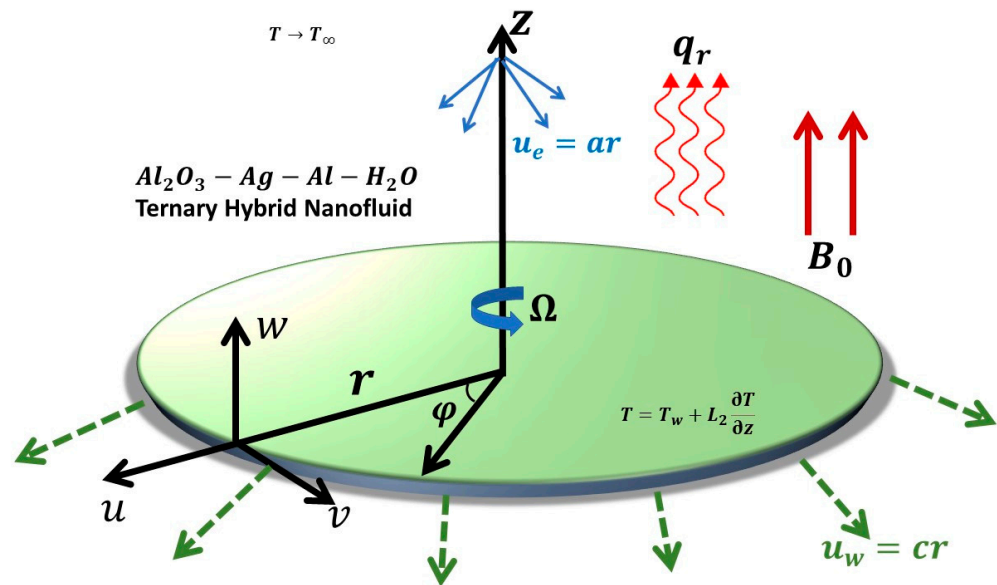


Figure 1. Physical configuration of the problem.

The axisymmetric, time-dependent, component equations are as follows (see [44,45]):

$$\frac{\partial u}{\partial r} + \frac{v}{r} + \frac{\partial w}{\partial z} = 0, \tag{7}$$

$$\rho_{tnl} \left( u \frac{\partial u}{\partial r} + w \frac{\partial u}{\partial z} - \frac{v^2}{r} \right) = -\frac{\partial p}{\partial r} + \mu_{tnl} \left( \frac{\partial^2 u}{\partial r^2} + \frac{1}{r} \frac{\partial u}{\partial r} - \frac{u}{r^2} + \frac{\partial^2 u}{\partial z^2} \right) - \sigma B_0^2 u, \tag{8}$$

$$\rho_{tnl} \left( u \frac{\partial v}{\partial r} + w \frac{\partial v}{\partial z} + \frac{uv}{r} \right) = \mu_{tnl} \left( \frac{\partial^2 v}{\partial r^2} + \frac{1}{r} \frac{\partial v}{\partial r} - \frac{v}{r^2} + \frac{\partial^2 v}{\partial z^2} \right) - \sigma B_0^2 v, \tag{9}$$

$$\rho_{tnl} \left( u \frac{\partial w}{\partial r} + w \frac{\partial w}{\partial z} \right) = -\frac{\partial p}{\partial z} + \mu_{tnl} \left( \frac{\partial^2 w}{\partial r^2} + \frac{1}{r} \frac{\partial w}{\partial r} + \frac{\partial^2 w}{\partial z^2} \right) \tag{10}$$

The prime focus of the study is to compare the three different forms of Rosseland’s radiative heat flux (namely, linear, quadratic, and full nonlinear forms) in the energy equation. More details of three different forms of Rosseland thermal radiation after boundary layer approximation are given in Chapter 2 of [33]. The energy equation with linear thermal radiation (LTR) is:

$$(\rho C_p)_{tnl} \left( u \frac{\partial T}{\partial r} + w \frac{\partial T}{\partial z} \right) = \left( k_{tnl} + \frac{16\sigma^* T_\infty^3}{3k^*} \right) \left( \frac{\partial^2 T}{\partial z^2} \right) + Q_t(T - T_\infty) + Q_e(T_w - T_\infty) \exp\left(-\frac{nz}{r} \sqrt{Re}\right) \tag{11}$$

with quadratic thermal radiation (QTR) is:

$$\begin{aligned}
 (\rho C_p)_{tnl} \left( u \frac{\partial T}{\partial r} + w \frac{\partial T}{\partial z} \right) &= \left( k_{tnl} - \frac{32\sigma^* T_\infty^3}{3k^*} \right) \left( \frac{\partial^2 T}{\partial z^2} \right) + \frac{48\sigma^* T_\infty^2}{3k^*} \left[ \left( \frac{\partial T}{\partial z} \right)^2 + T \frac{\partial^2 T}{\partial z^2} \right] + Q_t(T - T_\infty) \\
 &+ Q_e(T_w - T_\infty) \exp\left(-\frac{nz}{r} \sqrt{Re}\right)
 \end{aligned} \tag{12}$$

with full nonlinear thermal radiation (FNTR) is:

$$\begin{aligned}
 (\rho C_p)_{tnl} \left( u \frac{\partial T}{\partial r} + w \frac{\partial T}{\partial z} \right) &= k_{tnl} \left( \frac{\partial^2 T}{\partial z^2} \right) + \frac{16\sigma^* T_\infty^2}{3k^*} \left[ T^3 \frac{\partial^2 T}{\partial z^2} + 3T^2 \left( \frac{\partial T}{\partial z} \right)^2 \right] + Q_t(T - T_\infty) \\
 &+ Q_e(T_w - T_\infty) \exp\left(-\frac{nz}{r} \sqrt{Re}\right)
 \end{aligned} \tag{13}$$

Apposite multiple-slippage boundary conditions are as follows (see [18,19]):

$$u = cr + L_1 \frac{\partial u}{\partial z}, \quad v = r\Omega + L_1 \frac{\partial v}{\partial z}, \quad w = 0, \quad T = T_w + L_2 \frac{\partial T}{\partial z}, \quad \text{at } z = 0 \tag{14a}$$

$$u \rightarrow u_e = ar, \quad v \rightarrow v_e = 0, \quad w \rightarrow w_e = -2az, \quad T \rightarrow T_\infty \quad \text{as } z \rightarrow \infty \tag{14b}$$

where  $L_i$  ( $i = 1, 2$ ) are the slip coefficients.

As suggested by Animasaun et al. [7], the effective properties of  $H_2O - Al_2O_3 - Al - Ag$  nanofluid are listed below (see for more details [7–9]):

$$\rho_{tnl} = (1 - \phi)\rho_l + \phi_{np1}\rho_{np1} + \phi_{np2}\rho_{np2} + \phi_{np3}\rho_{np3}, \tag{15}$$

$$(\rho C_p)_{tnl} = (1 - \phi)(\rho C_p)_l + \phi_{np1}(\rho C_p)_{np1} + \phi_{np2}(\rho C_p)_{np2} + \phi_{np3}(\rho C_p)_{np3}, \tag{16}$$

$$\mu_{tnl} = \frac{\phi_{np1}\mu_{nl1} + \phi_{np2}\mu_{nl2} + \phi_{np3}\mu_{nl3}}{\phi}, \tag{17a}$$

$$\frac{\mu_{nl1}}{\mu_l} = 1 + 2.5\phi + 6.2\phi^2 \tag{17b}$$

$$\frac{\mu_{nl2}}{\mu_l} = 1 + 13.5\phi + 904.4\phi^2 \tag{17c}$$

$$\frac{\mu_{nl3}}{\mu_l} = 1 + 37.1\phi + 612.6\phi^2 \tag{17d}$$

$$k_{tnl} = \frac{\phi_{np1}k_{nl1} + \phi_{np2}k_{nl2} + \phi_{np3}k_{nl3}}{\phi}, \tag{18a}$$

$$\frac{k_{nl1}}{k_l} = \frac{k_{np1} + 2k_l - 2\phi(k_l - k_{np1})}{k_{np1} + 2k_l + \phi(k_l - k_{np1})} \tag{18b}$$

$$\frac{k_{nl2}}{k_l} = \frac{k_{np2} + 3.9k_l - 3.9\phi(k_l - k_{np2})}{k_{np2} + 2k_l + \phi(k_l - k_{np2})} \tag{18c}$$

$$\frac{k_{nl3}}{k_l} = \frac{k_{np3} + 4.7k_l - 4.7\phi(k_l - k_{np3})}{k_{np3} + 2k_l + \phi(k_l - k_{np3})} \tag{18d}$$

where subscripts  $l$ ,  $np1$ ,  $np2$ , and  $np3$  indicate base liquid, the volume fraction of silver NPs, the volume fraction of aluminum NPs, and the volume fraction of aluminum oxide NPs, respectively. The total fraction  $\phi$  is

$$\phi = \phi_{np1} + \phi_{np2} + \phi_{np3} \tag{19}$$

The thermophysical properties of nanoparticles are chosen from Animasaun et al. [7] and are valid at the temperature of 300 K. Ternary fluid is a composition of water, spherical-

shaped silver, cylindrical-shaped aluminum oxide, and platelet-shaped aluminum nanoparticles. Thus, the present results are not valid for other shapes of nanoparticles and valid for a temperature of 300 K.

The main aim of the present study is to obtain a self-similar solution by applying von Karman similarity variables. These similarity variables lead to dimensionless parameters and are useful to study the different forces acting on the system. Therefore, consider the von Karman variables:

$$F(\xi) = \frac{u}{rc}, \quad G(\xi) = \frac{v}{r\Omega}, \quad H(\xi) = \frac{\omega}{\sqrt{\Omega\nu_l}}, \quad \theta(\xi) = \frac{T - T_\infty}{T_w - T_\infty}, \quad \text{and } \xi = \frac{z}{r}\sqrt{Re} \quad (20)$$

The pressure gradient terms in (8) and (10) are eliminated using Bernoulli’s equation together with boundary layer approximations. Applying similarity variables to the governing equations led to the following ordinary differential equations system:

$$H' + 2F = 0, \quad (21)$$

$$F'' - A_1 \left( HF' + F^2 + \frac{Ha}{A_2}(F - \lambda) - G^2 - \lambda^2 \right) = 0, \quad (22)$$

$$G'' - A_1 \left( G'H + 2FG + \frac{Ha}{A_2}G \right) = 0, \quad (23)$$

$$(A_3 + Rd)\theta'' - PrA_4\theta'H + PrQ_T\theta + PrQ_E \exp(-n\xi) = 0, \quad (24a)$$

$$\{A_3 + Rd + 3Rd(\theta_r - 1)\theta\}\theta'' + 3Rd(\theta_r - 1)\theta'^2 - PrA_4\theta'H + PrQ_T\theta + PrQ_E \exp(-n\xi) = 0 \quad (24b)$$

$$[A_3 + Rd\{1 + (\theta_r - 1)\theta\}^3]\theta'' + 3Rd(\theta_r - 1)\{\theta(\theta_r - 1) + 1\}^2\theta'^2 - PrA_4\theta'H + PrQ_T\theta + PrQ_E \exp(-n\xi) = 0 \quad (24c)$$

$$H(\xi) = 0, \quad F(\xi) = 1 + \alpha_1 F'(\xi), \quad G(\xi) = \omega + \alpha_1 G'(\xi), \quad (25)$$

$$\theta(\xi) = 1 + \alpha_2 \theta'(\xi), \quad \text{at } \xi = 0$$

$$F(\xi) \rightarrow \lambda, \quad G(\xi) \rightarrow 0, \quad \theta(\xi) \rightarrow 0 \text{ as } \xi \rightarrow \infty \quad (26)$$

Here, we mention that Equation (24a–c) corresponds to the dimensionless energy equation for LTR, QTR, and FNTR cases, correspondingly. In the above system,  $Ha = \frac{\sigma B_0^2}{\rho_l a}$  denotes the magnetic parameter,  $Rd = \frac{4\sigma^* T_\infty^3}{3k_l k^*}$  denotes the radiation parameter,  $Pr = \frac{\mu_l C_{p_l}}{k_l}$  denotes the Prandtl number,  $\lambda = \frac{a}{c}$  denotes the stretching ratio,  $\theta_r = \frac{T_w}{T_\infty}$  denotes the temperature ratio,  $Q_T = \frac{Q_t}{(\rho C_p)_l c}$  denotes the THS number,  $Q_E = \frac{Q_e}{(\rho C_p)_l c}$  denotes the ESHS number,  $\alpha_1 = L_1 \sqrt{\frac{2\Omega}{\nu_l}}$  denotes the velocity slip parameter,  $\alpha_2 = L_2 \sqrt{\frac{2\Omega}{\nu_l}}$  denotes the thermal slip parameter, and  $\omega = \frac{\Omega}{c}$  denotes the rotation parameter and the symbols used for simplicity:

$$A_1 = \left( \frac{\phi A_2}{\phi_{np1} A_{11} + \phi_{np2} A_{12} + \phi_{np3} A_{13}} \right), \quad A_{11} = 1 + 2.5\phi + 6.2\phi^2,$$

$$A_{12} = 1 + 13.5\phi + 904.4\phi^2, \quad A_{13} = 1 + 37.1\phi + 612.6\phi^2,$$

$$A_2 = (1 - \phi) + \phi_{np1} \frac{\rho_{np1}}{\rho_l} + \phi_{np2} \frac{\rho_{np2}}{\rho_l} + \phi_{np3} \frac{\rho_{np3}}{\rho_l},$$

$$A_3 = \frac{\phi_{np1} A_{31} + \phi_{np2} A_{32} + \phi_{np3} A_{33}}{\phi}, \quad A_{31} = \frac{k_{np1} + 2k_l - 2\phi(k_l - k_{np1})}{k_{np1} + 2k_l + \phi(k_l - k_{np1})}$$

$$A_{32} = \frac{k_{np2} + 3.9k_l - 3.9\phi(k_l - k_{np2})}{k_{np2} + 3.9k_l + \phi(k_l - k_{np2})}, \quad A_{33} = \frac{k_{np3} + 4.7k_l - 4.7\phi(k_l - k_{np3})}{k_{np3} + 4.7k_l + \phi(k_l - k_{np3})}$$

$$A_4 = (1 - \phi) + \phi_{np1} \frac{(\rho C_p)_{np1}}{(\rho C_p)_l} + \phi_{np2} \frac{(\rho C_p)_{np2}}{(\rho C_p)_l} + \phi_{np3} \frac{(\rho C_p)_{np3}}{(\rho C_p)_l}.$$

The shear stress at  $z = 0$  along the tangential and radial directions is given by (see [44,45]):

$$\tau_\phi = \left[ \mu_{tnl} \left( \frac{\partial v}{\partial z} + \frac{1}{z} \frac{\partial w}{\partial \phi} \right) \right]_{z=0} \tag{27}$$

$$\tau_r = \left[ \mu_{tnl} \left( \frac{\partial u}{\partial z} + \frac{\partial w}{\partial r} \right) \right]_{z=0} \tag{28}$$

The total heat flux at  $z = 0$  is:

$$q_w = \left[ q_r - k_{tnl} \frac{\partial T}{\partial z} \right]_{z=0} \tag{29}$$

The wall-friction factors along the tangential and radial directions and the Nusselt number, Sherwood number, and local motile number are computed using (see [44,45]):

$$C_G = \frac{\tau_\phi}{\frac{1}{2} \rho_l (rc)^2} \tag{30}$$

$$C_F = \frac{\tau_r}{\frac{1}{2} \rho_l (rc)^2}, \tag{31}$$

$$Nu = \frac{rq_w}{k_l (T_w - T_\infty)} \tag{32}$$

Self-similar forms of (33)–(37) are given below:

$$Re^{1/2} C_G = \frac{\mu_{tnl}}{\mu l} G'(0) \tag{33}$$

$$Re^{1/2} C_F = \frac{\mu_{tnl}}{\mu l} F'(0), \tag{34}$$

$$Nur = Re^{-1/2} Nu = -(A_3 + Rd)\theta'(0), \tag{35a}$$

$$Nur = Re^{-1/2} Nu = -(A_3 + Rd + 3Rd(\theta_r - 1)(1 + \alpha_2\theta'(0)))\theta'(0), \tag{35b}$$

$$Nur = Re^{-1/2} Nu = -\left[ A_3 + Rd\{\theta_r + (\theta_r - 1)\alpha_2\theta'(0)\}^3 \right] \theta'(0), \tag{35c}$$

where  $Nur$  stands for reduced Nusselt number and  $Re = ru_w/\nu_l$  is the local Reynolds number. Equation (35a–c) corresponds to the dimensionless Nusselt number for the LTR, QTR, and FNTR cases, correspondingly.

### 3. Numerical Approach

Equations (21)–(26) do not possess analytical solutions as they are nonlinear and coupled. Therefore, the FEM is used to handle them for approximate solutions (more details are provided in [38–41]). In FEM, the problem is discretized into a finite number of elements and then consequent algebraic equations are solved. To this end, implement the variational formulations into (21)–(26) with an element  $\Omega_e = (\xi_e, \xi_{e+1})$ , and this leads to the following system:

$$\begin{bmatrix} [M^{11}] & [M^{12}] & [M^{13}] & [M^{14}] \\ [M^{21}] & [M^{22}] & [M^{23}] & [M^{24}] \\ [M^{31}] & [M^{32}] & [M^{33}] & [M^{34}] \\ [M^{41}] & [M^{42}] & [M^{43}] & [M^{44}] \end{bmatrix} \begin{bmatrix} H \\ F \\ G \\ \theta \end{bmatrix} = \begin{bmatrix} \{c\}^1 \\ \{c\}^2 \\ \{c\}^3 \\ \{c\}^4 \end{bmatrix} \tag{36}$$

where  $[M^{mn}]$  and  $\{c\}^m (m, n = 1, \dots, 4)$  are defined as:

$$M_{ij}^{11} = \int_{\bar{\zeta}_e}^{\bar{\zeta}_{e+1}} N_i \frac{dN_j}{d\bar{\zeta}} d\bar{\zeta}, \tag{37a}$$

$$M_{ij}^{12} = -2 \int_{\bar{\zeta}_e}^{\bar{\zeta}_{e+1}} N_i N_j d\bar{\zeta}, \tag{37b}$$

$$M_{ij}^{13} = 0, \tag{37c}$$

$$M_{ij}^{14} = 0, \tag{37d}$$

$$M_{ij}^{21} = 0, \tag{38a}$$

$$M_{ij}^{22} = - \int_{\bar{\zeta}_e}^{\bar{\zeta}_{e+1}} \frac{dN_i}{d\bar{\zeta}} \frac{dN_j}{d\bar{\zeta}} d\bar{\zeta} - A_1 \left\{ \int_{\bar{\zeta}_e}^{\bar{\zeta}_{e+1}} (N_i \bar{H} \frac{dN_j}{d\bar{\zeta}} + N_i \bar{F} N_j + \frac{Ha}{A_2} N_i N_j) d\bar{\zeta} \right\}, \tag{38b}$$

$$M_{ij}^{23} = A_1 \int_{\bar{\zeta}_e}^{\bar{\zeta}_{e+1}} N_i \bar{G} N_j d\bar{\zeta}, \tag{38c}$$

$$M_{ij}^{24} = 0, \tag{38d}$$

$$M_{ij}^{31} = 0, \tag{39a}$$

$$M_{ij}^{32} = -2A_1 \int_{\bar{\zeta}_e}^{\bar{\zeta}_{e+1}} N_i \bar{G} N_j d\bar{\zeta}, \tag{39b}$$

$$M_{ij}^{33} = - \int_{\bar{\zeta}_e}^{\bar{\zeta}_{e+1}} \frac{dN_i}{d\bar{\zeta}} \frac{dN_j}{d\bar{\zeta}} d\bar{\zeta} - A_1 \int_{\bar{\zeta}_e}^{\bar{\zeta}_{e+1}} N_i \bar{H} \frac{dN_j}{d\bar{\zeta}} d\bar{\zeta} - A_1 \frac{Ha}{A_2} \int_{\bar{\zeta}_e}^{\bar{\zeta}_{e+1}} N_i N_j d\bar{\zeta}, \tag{39c}$$

$$M_{ij}^{34} = 0, \tag{39d}$$

$$c_i^1 = 0, \tag{40a}$$

$$c_i^2 = - \left( N_i \frac{dF}{d\bar{\zeta}} \right)_{\bar{\zeta}_e}^{\bar{\zeta}_{e+1}}, \tag{40b}$$

$$c_i^3 = - \left( N_i \frac{dG}{d\bar{\zeta}} \right)_{\bar{\zeta}_e}^{\bar{\zeta}_{e+1}} \tag{40c}$$

For the LTR case,

$$M_{ij}^{41} = M_{ij}^{42} = M_{ij}^{43} = 0, \tag{41a}$$

$$M_{ij}^{44} = -(A_3 + Rd) \int_{\bar{\zeta}_e}^{\bar{\zeta}_{e+1}} \frac{dN_i}{d\bar{\zeta}} \frac{dN_j}{d\bar{\zeta}} d\bar{\zeta} - PrA_4 \int_{\bar{\zeta}_e}^{\bar{\zeta}_{e+1}} N_i \bar{H} \frac{dN_j}{d\bar{\zeta}} d\bar{\zeta} + PrQ_T \int_{\bar{\zeta}_e}^{\bar{\zeta}_{e+1}} N_i N_j d\bar{\zeta} \tag{41b}$$

$$c_i^4 = - \left( N_i (A_3 + Rd) \frac{d\theta}{d\bar{\zeta}} \right)_{\bar{\zeta}_e}^{\bar{\zeta}_{e+1}} - PrQ_E \int_{\bar{\zeta}_e}^{\bar{\zeta}_{e+1}} \exp(-n\bar{\zeta}) N_i d\bar{\zeta} \tag{41c}$$

For the QTR case,

$$M_{ij}^{41} = M_{ij}^{42} = M_{ij}^{43} = 0, \tag{42a}$$

$$M_{ij}^{44} = - \int_{\bar{\zeta}_e}^{\bar{\zeta}_{e+1}} \frac{dN_i}{d\bar{\zeta}} \frac{dN_j}{d\bar{\zeta}} (A_3 + Rd + 3Rd(\theta_r - 1)\bar{\theta}) d\bar{\zeta} - PrA_4 \int_{\bar{\zeta}_e}^{\bar{\zeta}_{e+1}} N_i \bar{H} \frac{dN_j}{d\bar{\zeta}} d\bar{\zeta} + PrQ_T \int_{\bar{\zeta}_e}^{\bar{\zeta}_{e+1}} N_i N_j d\bar{\zeta} \tag{42b}$$

$$c_i^4 = - \left( N_i (A_3 + Rd + 3Rd(\theta_r - 1)\bar{\theta}) \frac{d\theta}{d\bar{\zeta}} \right)_{\bar{\zeta}_e}^{\bar{\zeta}_{e+1}} - PrQ_E \int_{\bar{\zeta}_e}^{\bar{\zeta}_{e+1}} \exp(-n\bar{\zeta}) N_i d\bar{\zeta}, \tag{42c}$$

For the FNTR case,

$$M_{ij}^{41} = M_{ij}^{42} = M_{ij}^{43} = 0, \tag{43a}$$

$$M_{ij}^{44} = - \int_{\xi_e}^{\xi_{e+1}} \frac{dN_i}{d\xi} \left( A_3 + Rd \{ 1 + (\theta_r - 1) \bar{\theta} \}^3 \right) \frac{dN_j}{d\xi} d\xi - Pr A_4 \int_{\xi_e}^{\xi_{e+1}} N_i \bar{H} \frac{dN_j}{d\xi} d\xi + Pr Q_T \int_{\xi_e}^{\xi_{e+1}} N_i N_j d\xi, \quad (43b)$$

$$c_i^4 = - \left( N_i \left( A_3 + Rd \{ 1 + (\theta_r - 1) \bar{\theta} \}^3 \right) \frac{d\bar{\theta}}{d\xi} \right)_{\xi_e}^{\xi_{e+1}} - Pr Q_E \int_{\xi_e}^{\xi_{e+1}} \exp(-n\xi) N_i d\xi. \quad (43c)$$

where  $\bar{\Theta} = \sum_{i=1}^2 \bar{\Theta}_i N_i$  and  $\Theta (F, G, \theta)$  is a dependent variable and  $N_i$  is a linear shape function. Subsequent linear equations are solved with an accuracy of  $10^{-8}$  using the Gauss elimination method. Table 1 presents the comparison of our FEM results with those reported in [18,19], and good agreement is noticed.

**Table 1.** Comparison of the FEM results with those in Irfan Mustafa et al. [19] and Turkyilmazoglu [18] for  $\lambda = \phi = Rd = \alpha_1 = \alpha_2 = Q_T = Q_E = 0$  and  $Pr = 1$ .

Ha	$\omega$	Present Results (FEM)			Irfan Mustafa et al. [19]			Turkyilmazoglu [18]		
		F'(0)	-G'(0)	-\theta'(0)	F'(0)	-G'(0)	-\theta'(0)	F'(0)	-G'(0)	-\theta'(0)
0	0	-1.173721	0	0.851998	-1.1737	0	0.852	-1.1737	0	0.852
	1	-0.948314	1.486952	0.875663	-0.9483	1.487	0.8757	-0.9483	1.487	0.8757
	2	-0.326244	3.127827	0.930411	-0.3263	3.1278	0.9304	-0.3262	3.1278	0.9304
	5	3.193732	9.253538	1.129141	3.1937	9.2536	1.1292	3.1937	9.2535	1.1291
	10	12.72090	22.913401	1.425927	12.7206	22.9139	1.426	12.7209	22.9134	1.4259
	20	40.90735	59.686430	1.874175	40.9056	59.6895	1.8743	40.9057	60.0129	1.8944
2	0	-1.830489	0	0.726113	-1.8305	0	0.7261	-1.8305	0	0.7261
	1	-1.663452	2.023942	0.742231	-1.6635	2.0239	0.7422	-1.6634	2.0239	0.7422
	2	-1.175346	4.113492	0.785373	-1.1754	4.1135	0.7854	-1.1753	4.1135	0.7854
	5	1.892947	11.140596	0.980285	1.8928	11.1407	0.9803	1.8929	11.1406	0.9803
	10	10.83338	25.722553	1.299221	10.8329	25.7231	1.2993	10.8334	25.7225	1.2992
	20	38.18798	64.060430	1.797315	38.1857	64.0635	1.7974	38.188	64.0604	1.7973

### 4. Results and Discussion

Numerical computation of the von Karman three-dimensional flow problem for ternary hybrid nanofluid ( $H_2O - Al_2O_3 - Al - Ag$ ) subject to non-uniform heat sources (temperature-related heat source (THS) and exponential space-related heat source (ESHS)) using FEM is performed. The main emphasis is given to the comparison of thermal characteristics under three different forms of Rosseland thermal radiation (LTR, QTR, and FNTR cases). The effects of the Hartmann parameter ( $Ha$ ), radiation parameter ( $Rd$ ), rotation parameter ( $\omega$ ), velocity slip number ( $\alpha_1$ ), THS number ( $Qt$ ), temperature ratio ( $\theta_r$ ), ESHS number ( $Qe$ ), and temperature slip number ( $\alpha_2$ ) are scrutinized for 1% of cylindrical aluminum oxide ( $Al_2O_3$ ), spherical aluminum ( $Al$ ), and platelet silver ( $Ag$ ) nanoparticles (NPs). The computations are made for  $Ha = \lambda = \omega = Rd = 0.5$ ,  $\theta_r = 2$ ,  $\alpha_1 = 0.4$ ,  $\alpha_2 = 0.6$ ,  $Qt = Qe = 0.1$  and  $Pr = 6.0674$ .

Figures 2–4 are designed to analyze the effects of the Hartmann number ( $Ha$ ), rotation parameter ( $\omega$ ), THS number ( $Qt$ ), ESHS number ( $Qe$ ), radiation parameter ( $Rd$ ), and temperature slip number ( $\alpha_2$ ) on the temperature distribution ( $\theta(\xi)$ ) for the LTR, QTR and FNTR cases. In these figures, the solid curves represent the LTR results calculated using Equation (23a), the dashed curves represent the QTR results calculated using Equation (23b) and the dashed curves represent the FNTR results calculated using Equation (23c). At a fixed value of other parameters, as the magnetic field strength  $Ha$  increases, the temperature distribution  $\theta(\xi)$  increases along with the thickness of the temperature layer (see Figure 2a). As the magnetism parameter increases, the increase in the Lorentz force progressively accelerates. As the movement of the fluid slows down and allows the fluid to

absorb more and more heat, as a result, the temperature distribution is improved. Figure 2b depicts that temperature distribution  $\theta(\xi)$  reduces for cumulative values of the rotation parameter ( $\omega$ ). As the rotation parameter rises, the Coriolis force in the system upsurges. As a result, the thermal energy distribution  $\theta(\xi)$  escalated throughout the boundary layer.

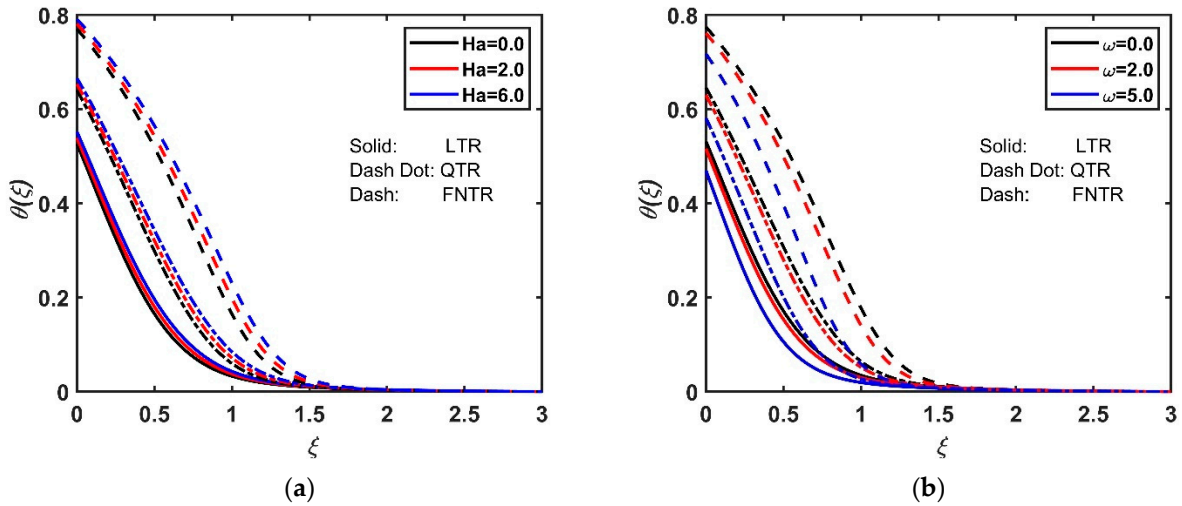


Figure 2. Impact of (a)  $Ha$  on  $\theta(\xi)$ , and (b)  $\omega$  on  $\theta(\xi)$  for the LTR, QTR and FNTR cases.

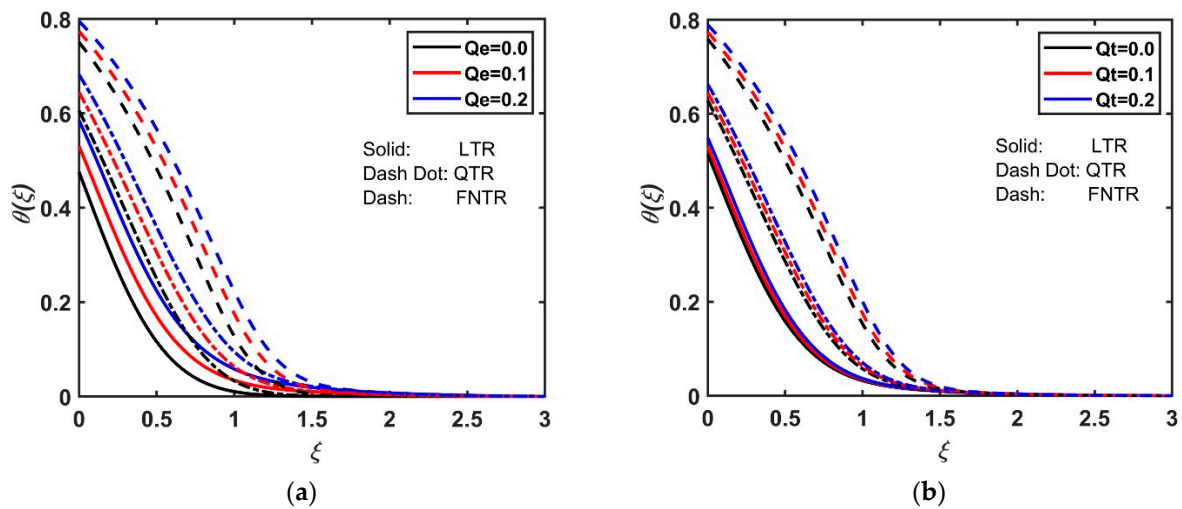


Figure 3. Impact of (a)  $Qe$  on  $\theta(\xi)$ , and (b)  $Qt$  on  $\theta(\xi)$  for the LTR, QTR and FNTR cases.

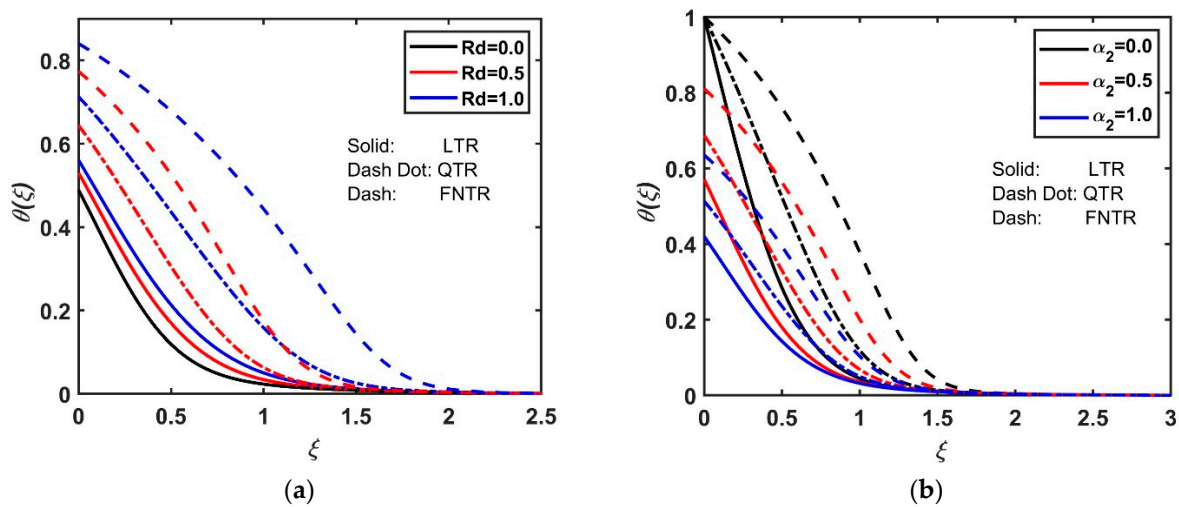


Figure 4. Impact of (a)  $Rd$  on  $\theta(\xi)$ , and (b)  $\alpha_2$  on  $\theta(\xi)$  for LTR, QTR and FNTR cases.

The behavior of the distribution of thermal energy  $\theta(\xi)$  for the impact of THS and ESHS is portrayed in Figure 3a,b, selecting both  $Qt$  and  $Qe$  as 0, 0.1, and 0.2. In these figures,  $Qt = 0$  and  $Qe = 0$  represent the absence of internal heat sources. It has been revealed that, among THS and ESHS, the ESHS has substantial backing on the growth of the temperature boundary layer. As expected,  $\theta(\xi)$  rises across the boundary layer region for cumulative values of both  $Qt$  and  $Qe$ . Mathematically, the terms  $PrQ_T\theta$  and  $PrQ_E \exp(-n\xi)$  supplement to the growth of  $\theta$  values. Physically, the heat source phenomenon adds extra heat internally into the flow system and, subsequently, the growth of the thermal layer escalated. Furthermore, the impact of internal heat sources is comparatively protuberant in the FNTR case compared to other cases. The behavior of the thermal energy  $\theta(\xi)$  for various radiation and thermal slip numbers is portrayed in Figure 4a,b, selecting both  $Rd$  and  $\alpha_2$  as 0, 0.5, and 1.0. The temperature on the disk surface attained its maximum when  $Rd$  is maximum and in the case of FNTR. The radiation feature is comparatively protuberant for the FNTR case compared to the QTR and LTR cases. As the radiation parameter values elevated, the thermal energy distribution was exaggerated in the region of the thermal layer. Physically, as  $Rd$  value increases, the radiative heat flux in the system upsurges, due to which  $\theta(\xi)$  increases. However, the  $\theta(\xi)$  is greater on the surface of the disk. Furthermore,  $Rd = 0$  represents the absence of thermal radiation in which the thermal energy  $\theta(\xi)$  is minimal across the region of the boundary layer. Furthermore,  $\theta(\xi)$  reduces for cumulative values of  $\alpha_2$  (see Figure 4b). When  $\alpha_2 = 0$ , this epitomizes the isothermal condition and the temperature  $\theta(\xi)$  in the disk remains as a unit value for distinct forms of Rosseland thermal radiation (LTR, QTR, and FNTR cases).

Figure 5a,b shows the radial velocity ( $F(\xi)$ ), and azimuthal velocity ( $G(\xi)$ ) for distinct values of the Hartmann number ( $Ha$ ). As the values of  $Ha$  increase, both radial and azimuthal velocity distributions upsurged. As the values of  $Ha$  increased, the intensity of the Lorentz force in the flow domain intensified. The Lorentz force hinders the movement of the fluid as a result, and the velocity field is reduced. The impact of the rotation parameter ( $\omega$ ) on  $F(\xi)$  and  $G(\xi)$  is described in Figure 6, since the rotation parameter ( $\omega$ ) increases the velocity throughout the region. Physically, the rotation of the disk improves the propulsion of the ternary nanofluid which, in turn, increases the velocity along the axial and azimuth directions. The phenomenon of disk rotation helps to control the rheological aspects of the ternary nanofluid. Figure 7 illustrates the role of velocity slip conditions on radial velocity ( $F(\xi)$ ), and azimuthal velocity ( $G(\xi)$ ). As expected, the velocity layer becomes thinner for higher sliding conditions on the disk surface.

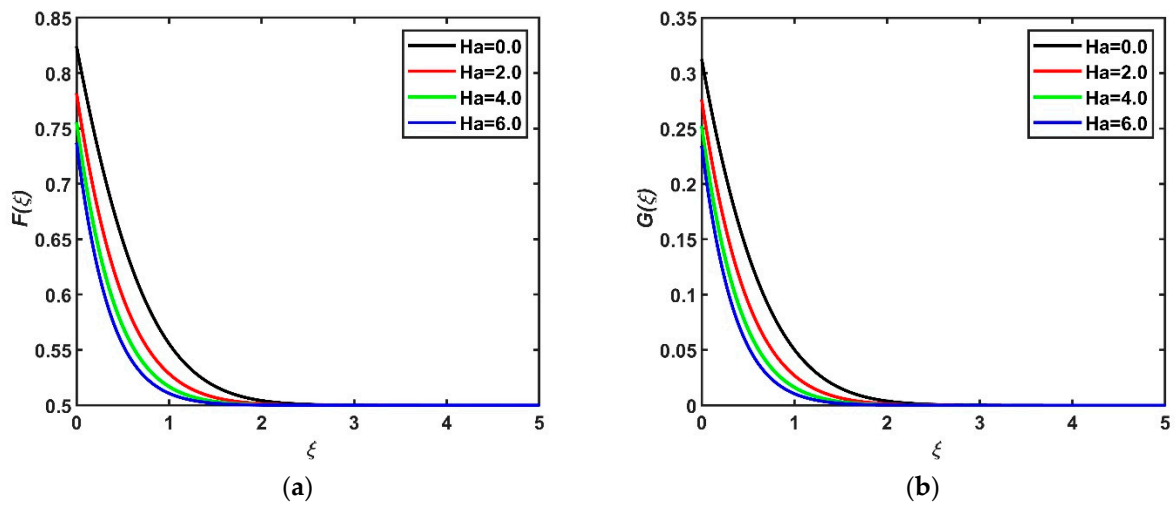


Figure 5. Impact of  $Ha$  on (a)  $F(\xi)$  and (b)  $G(\xi)$ .

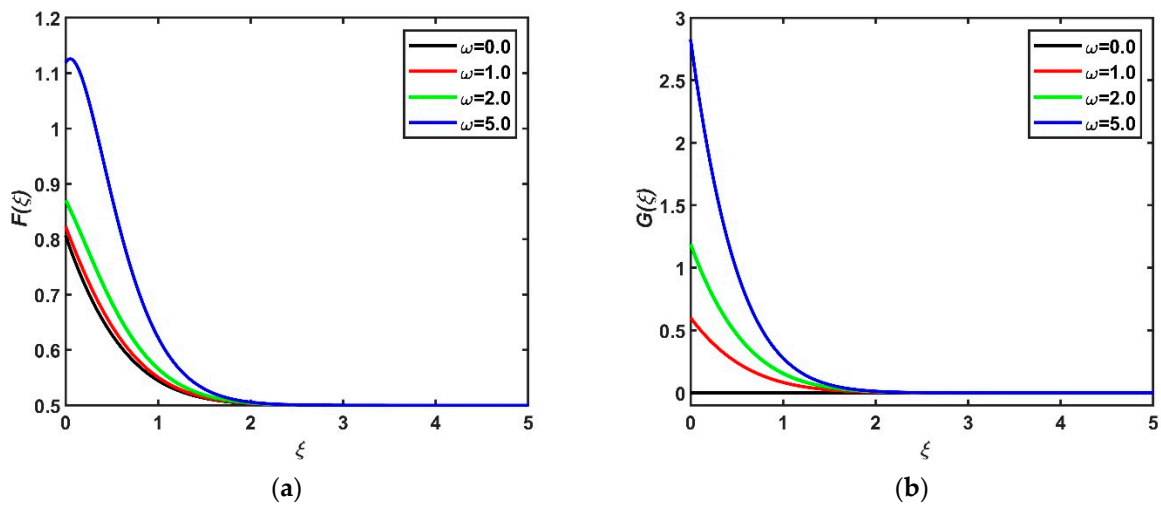


Figure 6. Impact of  $\omega$  on (a)  $F(\xi)$  and (b)  $G(\xi)$ .

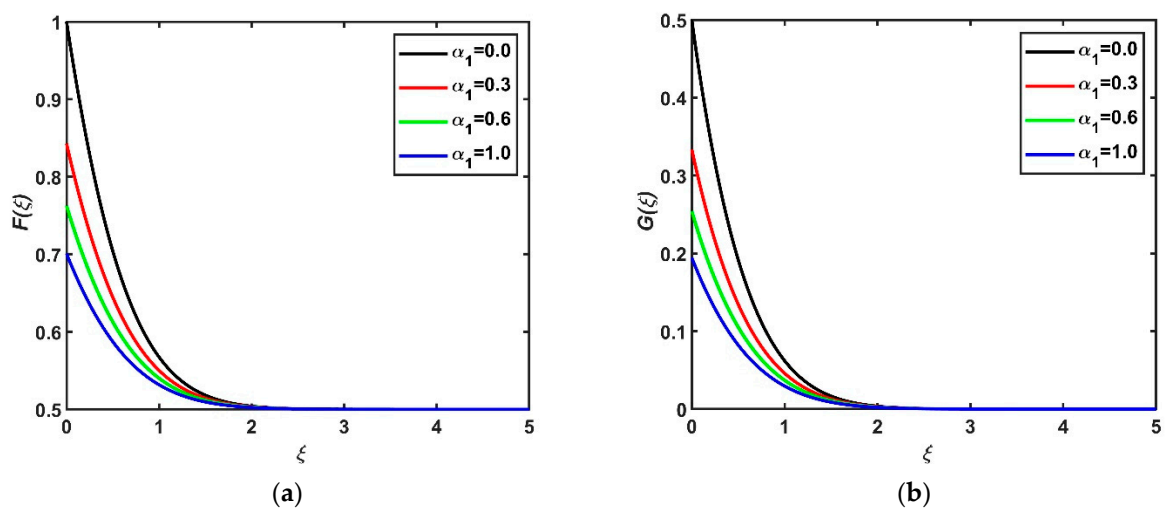


Figure 7. Impact of  $\alpha_1$  on (a)  $F(\xi)$  and (b)  $G(\xi)$ .

The impacts of  $Q_e$ ,  $Q_t$ ,  $Rd$  and  $\alpha_2$  on the reduced Nusselt number ( $Nur$ ) to examine the heat transport for LTR, QTR and FNTR are presented through contour plots (see Figure 8). As seen in Figure 8, by increasing the values of  $Q_e$  and  $Q_t$ , the reduced Nusselt number ( $Nur$ ) was reduced for all cases of LTR, QTR and FNTR. As the temperature layer becomes thinner for higher values of  $Q_e$  and  $Q_t$ , consequently, the rate of heat transport at the surface of the disk decreases. It is also seen that the  $Nur$  values have reached the maximum for high values of  $\alpha_2$  and relatively low values of  $Rd$ . Furthermore, the  $Nur$  values are maximum for the FNTR case compared to the QTR and LTR cases.

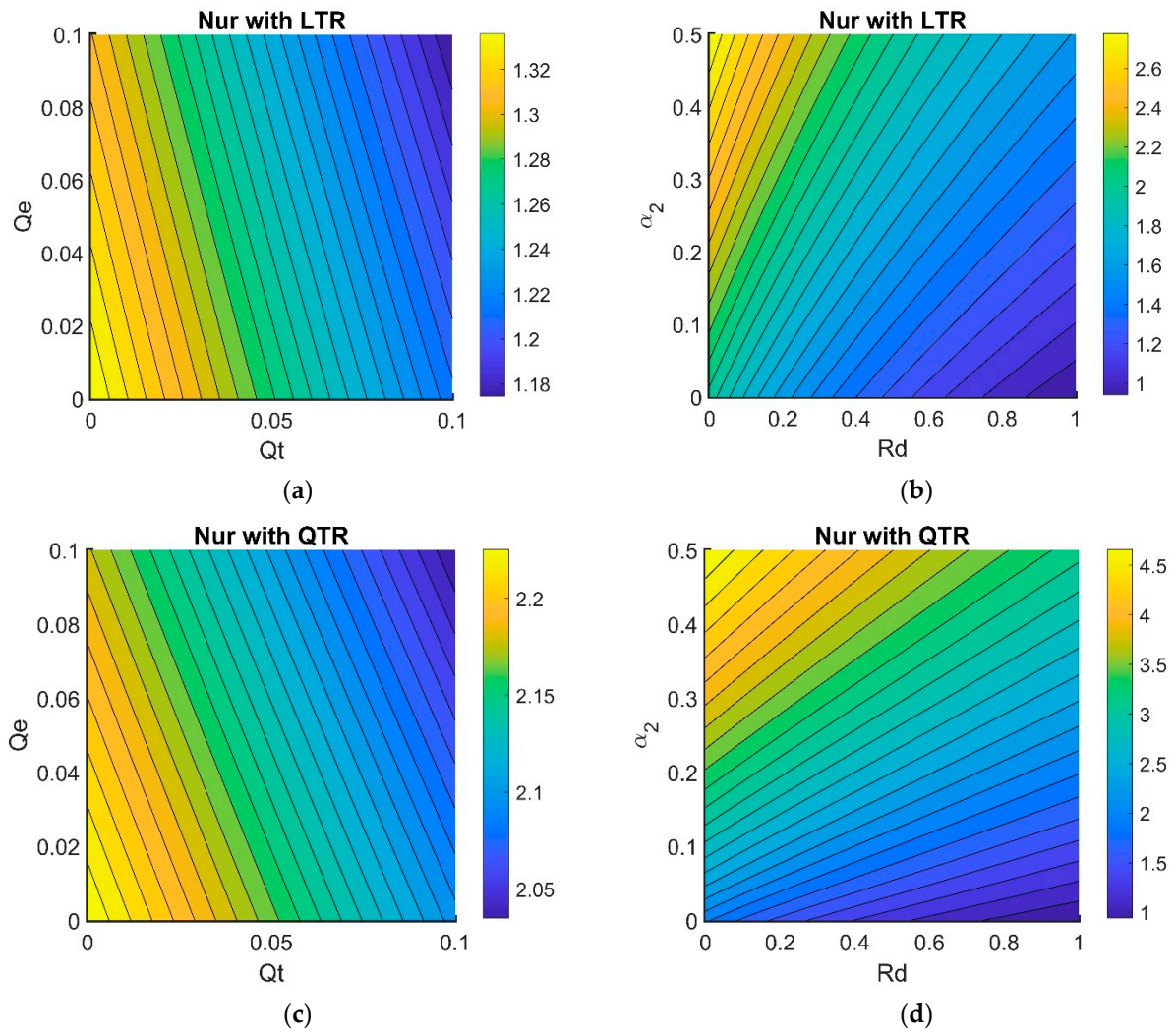


Figure 8. Cont.

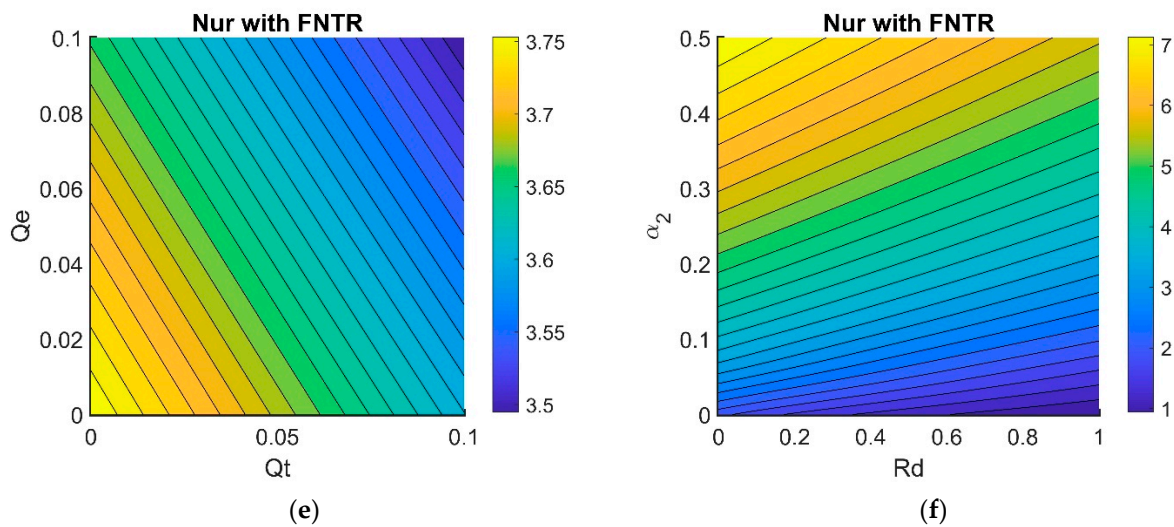


Figure 8. (a–f): Impact of  $Qe$  &  $Qt$  and  $Rd$  &  $\alpha_2$  on  $Nur$  for the LTR, QTR and FNTR cases.

Table 2 exhibits the influence of disk rotation on the radial shear stress ( $\frac{\mu_{tnl}}{\mu_l} F'(0)$ ) and torque ( $-\frac{\mu_{tnl}}{\mu_l} G'(0)$ ) in the presence and absence of composite nanoparticles. In compliance with our previous results, the higher the rotation number, the larger the shear stresses. In addition, the shear stress along the axial and azimuth directions was less when the disk stopped rotating. Table 3 presents the  $\frac{\mu_{tnl}}{\mu_l} F'(0)$  and  $-\frac{\mu_{tnl}}{\mu_l} G'(0)$  values for discrete values of  $Ha$  for clean and ternary fluids. It is observed that the radial shear stress ( $\frac{\mu_{tnl}}{\mu_l} F'(0)$ ) becomes lower in the presence of a magnetic field, whereas  $-\frac{\mu_{tnl}}{\mu_l} G'(0)$  is lower for nonmagnetic ternary fluid. From Tables 2 and 3, the shear stresses are greater for ternary nanofluid ( $H_2O - Al_2O_3 - Al - Ag$ ) than for the clean fluid ( $H_2O$ ).

Table 2. The values of  $\frac{\mu_{tnl}}{\mu_l} F'(0)$ , and  $-\frac{\mu_{tnl}}{\mu_l} G'(0)$  for different values of  $\omega$ .

$\omega$	Ordinary Fluid		Ternary Hybrid Nanofluid	
	$\frac{\mu_{tnl}}{\mu_l} F'(0)$	$-\frac{\mu_{tnl}}{\mu_l} G'(0)$	$\frac{\mu_{tnl}}{\mu_l} F'(0)$	$-\frac{\mu_{tnl}}{\mu_l} G'(0)$
0	-0.48335771	0	-0.80181321	0
0.5	-0.47267704	0.49575328	-0.78005578	0.82705398
1	-0.44127131	0.99612731	-0.71609273	1.66346764
2	-0.32387576	2.02544265	-0.47705420	3.39391449
5	0.29644174	5.43355235	0.79109231	9.22650722
10	1.62531874	11.9972247	3.55128606	20.72895781

Table 3. The values of  $\frac{\mu_{tnl}}{\mu_l} F'(0)$ , and  $-\frac{\mu_{tnl}}{\mu_l} G'(0)$  for different values of  $Ha$ .

$Ha$	Ordinary Fluid		Ternary Hybrid Nanofluid	
	$\frac{\mu_{tnl}}{\mu_l} F'(0)$	$-\frac{\mu_{tnl}}{\mu_l} G'(0)$	$\frac{\mu_{tnl}}{\mu_l} F'(0)$	$-\frac{\mu_{tnl}}{\mu_l} G'(0)$
0	-0.44000805	0.46833571	-0.72812791	0.78341243
1	-0.50045179	0.51971352	-0.82555654	0.86619275
2	-0.54567020	0.55984084	-0.90225322	0.93384518
5	-0.63580852	0.64310922	-1.06445868	1.08249169
10	-0.72164089	0.72523676	-1.22988132	1.23960372
20	-0.81295698	0.81447006	-1.41722049	1.42170302

Table 4 exhibits the radiation effects on  $Nur$  of clean fluid and ternary fluid for the LTR, QTR, and FNTR cases. The radiation phenomenon causes a deterioration in the behavior of heat transport ( $Nur$ ). Also, the  $Nur$  is higher for the  $H_2O - Al_2O_3 - Al - Ag$  ternary fluid than the  $H_2O$  clean fluid. Tables 5 and 6 are presented to compare the consequence of THS and ESHS on  $Nur$  for the cases of LTR, QTR, and FNTR. The  $Nur$  becomes augmented to increase in the  $Qt$  and  $Qe$  values. The variation of  $Nur$  is more evident for higher  $Qe$  values than  $Qt$ . Furthermore, the  $Nur$  value attained its maximum in the FNTR case compared to the QTR and LTR cases.

**Table 4.**  $Nur$  values versus  $Rd$  for the LTR, QTR, and FNTR cases.

$Rd$	Ternary Hybrid Nanofluid			Ordinary Fluid		
	LTR	QTR	FNTR	LTR	QTR	FNTR
0	0.15091875	0.15091875	0.15091875	0.05445781	0.05445781	0.05445781
0.1	0.17995238	0.24000444	0.29735945	0.07998212	0.13362429	0.18632552
0.2	0.20901834	0.32747204	0.43718884	0.10578007	0.21300510	0.31494829
0.3	0.23805570	0.41287182	0.57063906	0.13174893	0.29127314	0.43846205
0.4	0.26701725	0.49610146	0.69830505	0.15780823	0.36796898	0.55692548

**Table 5.**  $Nur$  values versus  $Qt$  for the LTR, QTR, and FNTR cases.

$Qt$	Ternary Hybrid Nanofluid			Ordinary Fluid		
	LTR	QTR	FNTR	LTR	QTR	FNTR
0	0.79588316	1.20631721	1.53242058	0.69972271	1.10659613	1.43171775
0.03	0.77345459	1.17869507	1.50220551	0.67709330	1.07814361	1.40017445
0.05	0.75809732	1.15973799	1.48139333	0.66157103	1.05857777	1.37840077
0.07	0.7424036	1.14033011	1.46002499	0.64568557	1.03851389	1.35600646
0.09	0.72636188	1.12045629	1.43808131	0.62942404	1.01793444	1.33296913

**Table 6.**  $Nur$  values versus  $Qe$  for the LTR, QTR, and FNTR cases.

$Qe$	Ternary Hybrid Nanofluid			Ordinary Fluid		
	LTR	QTR	FNTR	LTR	QTR	FNTR
0	1.24641322	1.63250225	1.91053090	1.143942226	1.528179426	1.80588358
0.03	1.18938033	1.57415993	1.85447686	1.086339262	1.468735168	1.748172095
0.05	1.15135844	1.53485444	1.81633487	1.047937272	1.428627273	1.708811472
0.07	1.11333651	1.49522849	1.77758997	1.009535296	1.388148552	1.668764217
0.09	1.07531456	1.4552881	1.73825741	0.971133316	1.347308633	1.628058621

### 5. Concluding Remarks

The comparative study of linear (LTR), quadratic (QTR), and nonlinear radiation (FNTR) effects on the characteristics of heat transport subject to THS, magnetism, and ESHS for the stagnation-point three-dimensional transport of  $H_2O - Al_2O_3 - Al - Ag$  was performed. The single-phase fluid model and generalized slip conditions were implemented. The self-similarity governing equations were solved using the FEM. The key findings are as follows:

- With an increase in the rotation of the disk, both the axial and azimuth velocities increased significantly; consequently, the thickness of the layers widened.
- The magnetic parameter resulted in a deteriorated velocity of the ternary nanofluids; consequently, a decay in the velocity layer on the disk surface is noted.

- The nonlinear form of Rosseland thermal radiation possesses a maximum heat transport rate at the disk compared to the other two forms of thermal radiation.
- The phenomenon of exponential heat source has a substantial and positive effect on the thermal field compared to the phenomenon of a temperature-dependent heat source.
- For a lower radiation parameter and a higher thermal slip parameter, the Nusselt number has attained a maximum.
- For a maximum Nusselt number, both heat sources maintained as relatively small.
- Radial shear stress is minimal when the disk does not rotate.

The present study explored some interesting flow and heat transport phenomena on a rotating and stretching disk surface. The heat transport phenomenon with the appearance of thermal radiation finds applications in nuclear power plants, solar systems, astrophysical flows, gas production, spacecraft, electricity generation, etc. Therefore, the present study may find relevance in solar collectors, nuclear reactors, and applications involving heating and cooling processes. However, attention has been confined to Newtonian ternary nanofluid to explore the three different forms of Rosseland thermal radiation. Future studies may consider non-Newtonian fluids and different thermal boundary conditions and will be communicated imminently.

**Author Contributions:** P.R.: conceptualization, methodology, writing—original draft preparation, validation; G.G.: formal analysis, software, writing—review and editing, resources. All authors have read and agreed to the published version of the manuscript.

**Funding:** This study was supported by Internal Research Support Programs (Program No. IR-SPG202104), Wenzhou-Kean University, China.

**Conflicts of Interest:** The authors declare no conflict of interest.

## Nomenclature

$a, c$	positive constants
$\vec{B}$	magnetic field vector
$B_0$	magnetic field of uniform strength
$C_F$	wall friction along the radial direction
$C_p$	specific heat
$C_G$	wall friction in the azimuth direction
$\hat{e}_r, \hat{e}_\phi, \hat{e}_z$	unit vectors
$F, G, H$	dimensionless radial, azimuth, and axial velocity
$Ha$	magnetic parameter
$\vec{J}$	current density vector
$k^*$	Rosseland mean absorption
$k$	thermal conductivity ( $\text{Wm}^{-1}\text{K}^{-1}$ )
$L_1$	velocity slip coefficient
$L_2$	thermal slip coefficient
$n$	exponential index
$Nur$	reduced Nusselt number
$Nu$	Nusselt number
$Pr$	Prandtl number
$p$	pressure ( $\text{Nm}^{-2}$ )
$q_w$	heat flux at the disk surface ( $\text{Wm}^{-2}$ )
$q'''$	non-uniform heat source
$Q_t$	coefficient of temperature-dependent heat source
$Q_e$	coefficient of exponential space-dependent heat source
$Q_T$	temperature-dependent heat source parameter
$Q_E$	exponential space-dependent heat source parameter
$Rd$	radiation parameter
$Re$	Reynolds number
$t$	Time

$T$	fluid temperature (K)
$\vec{U}$	velocity vector (m/s)
$u, v, w$	velocity components along $r, \varphi, z$ directions (m/s)
$u_e, v_e, w_e$	free-stream velocities along $r, \varphi, z$ directions (m/s)
$u_w$	stretching velocity (m/s)
$r, \varphi, z$	cylindrical coordinates in radial, azimuthal, and tangential directions
Acronyms	
LTR	linear thermal radiation
QTR	quadratic thermal radiation
FNTR	full nonlinear thermal radiation
NPs	nanoparticles
Greek symbols	
$\nu$	kinematic viscosity ( $\text{m}^2\text{s}^{-1}$ )
$\sigma$	electrical conductivity
$\sigma^*$	Stefan–Boltzmann constant
$\theta_r$	temperature ratio
$\theta$	dimensionless temperature
$\mu$	dynamic viscosity ( $\text{kgm}^{-1}\text{s}^{-1}$ )
$\rho$	density ( $\text{kgm}^{-3}$ )
$\Omega$	angular velocity ( $\text{s}^{-1}$ )
$\lambda$	stretching ratio
$\xi$	similarity variable
$\alpha_1$	velocity slip parameter
$\alpha_2$	thermal slip parameter
$\omega$	rotation parameter
$\phi$	nanoparticle volume fraction
$\tau_r, \tau_\varphi$	radial and azimuthal wall shear stress
$\Omega_e$	finite element
$\rho C_p$	fluid heat capacity ( $\text{Jm}^{-3}\text{K}^{-1}$ )
Subscripts	
$tnl$	ternary nanofluid
$l$	water (liquid)
$w$	wall (disk surface)
$\infty$	ambient state
$np1$	volume fraction of aluminum oxide nanoparticles
$np2$	volume fraction of alumina nanoparticles
$np3$	volume fraction of silver nanoparticles
$n11$	aluminum oxide nanoliquid
$n12$	alumina nanoliquid
$n13$	silver nanoliquid

## References

1. Das, S.K.; Choi, S.U.; Patel, H.E. Heat transfer in nanofluids—A review. *Heat Transf. Eng.* **2006**, *27*, 3–19. [[CrossRef](#)]
2. Saidur, R.; Leong, K.Y.; Mohammed, H.A. A review on applications and challenges of nanofluids. *Renewable and Sustainable Energy Rev.* **2011**, *15*, 1646–1668. [[CrossRef](#)]
3. Yu, W.; Xie, H. A review on nanofluids: Preparation, stability mechanisms, and applications. *J. Nanomater.* **2012**, 1687–4110. [[CrossRef](#)]
4. Sahoo, R.R.; Kumar, V. Impact of novel dissimilar shape ternary composition-based hybrid nanofluids on the thermal performance analysis of radiator. *J. Therm. Sci. Eng. Appl.* **2021**, *13*, 1–23. [[CrossRef](#)]
5. Adun, H.; Kavaz, D.; Dagbasi, M. Review of ternary hybrid nanofluid: Synthesis, stability, thermophysical properties, heat transfer applications, and environmental effects. *J. Clean. Prod.* **2021**, *328*, 129525. [[CrossRef](#)]
6. Elnaqeeb, T.; Animsaun, I.L.; Shah, N.A. Ternary-hybrid nanofluids: Significance of suction and dual-stretching on three-dimensional flow of water conveying nanoparticles with various shapes and densities. *Z. Für Nat. A.* **2021**, *76*, 231–243. [[CrossRef](#)]
7. Animsaun, I.L.; Yook, S.J.; Muhammad, T.; Mathew, A. Dynamics of ternary-hybrid nanofluid subject to magnetic flux density and heat source or sink on a convectively heated surface. *Surf. Interfaces* **2022**, *28*, 101654. [[CrossRef](#)]
8. Shah, N.A.; Wakif, A.; El-Zahar, E.R.; Thumma, T.; Yook, S.J. Heat transfers thermodynamic activity of a second-grade ternary nanofluid flow over a vertical plate with Atangana-Baleanu time-fractional integral. *Alex. Eng. J.* **2022**, *61*, 10045–10053. [[CrossRef](#)]

9. Oke, A.S. Heat and Mass Transfer in 3D MHD Flow of EG-Based Ternary Hybrid Nanofluid Over a Rotating Surface. *Arab. J. Sci. Eng.* **2022**, 1–17. [[CrossRef](#)]
10. Ramesh, G.K.; Madhukesh, J.K.; Shehzad, S.A.; Rauf, A. Ternary nanofluid with heat source/sink and porous medium effects in stretchable convergent/divergent channel. *Proc. Inst. Mech. Eng. Part E J. Process Mech. Eng.* **2022**, 09544089221081344. [[CrossRef](#)]
11. Shah, N.A.; Wakif, A.; El-Zahar, E.R.; Ahmad, S.; Yook, S.J. Numerical simulation of a thermally enhanced EMHD flow of a heterogeneous micropolar mixture comprising (60%)-ethylene glycol (EG),(40%)-water (W), and copper oxide nanomaterials (CuO). *Case Stud. Therm. Eng.* **2022**, *35*, 102046. [[CrossRef](#)]
12. Sajjan, K.; Shah, N.A.; Ahamad, N.A.; Raju, C.S.K.; Kumar, M.D.; Weera, W. Nonlinear Boussinesq and Rosseland approximations on 3D flow in an interruption of Ternary nanoparticles with various shapes of densities and conductivity properties. *AIMS Math.* **2022**, *7*, 18416–18449. [[CrossRef](#)]
13. Priyadharshini, P.; Archana, M.V.; Ahammad, N.A.; Raju, C.S.K.; Yook, S.J.; Shah, N.A. Gradient descent machine learning regression for MHD flow: Metallurgy process. *Int. Commun. Heat Mass Transf.* **2022**, *138*, 106307. [[CrossRef](#)]
14. Kármán, T.V. Über laminare und turbulente Reibung. *ZAMM-J. Appl. Math. Mech./Z. Für Angew. Math. Und Mech.* **1921**, *1*, 233–252. [[CrossRef](#)]
15. Schlichting, H. *Boundary-Layer Theory*; McGraw-Hill: New York, NY, USA, 1979.
16. White, F.M. *Viscous Fluid Flow*; McGraw-Hill: New York, NY, USA, 1991.
17. Jensen, K.F.; Einset, E.O.; Fotiadis, D.I. Flow phenomena in chemical vapor deposition of thin films. *Annu. Rev. Fluid Mech.* **1991**, *23*, 197–232. [[CrossRef](#)]
18. Turkyilmazoglu, M. Three dimensional MHD stagnation flow due to a stretchable rotating disk. *Int. J. Heat Mass Transf.* **2012**, *55*, 6959–6965. [[CrossRef](#)]
19. Mustafa, I.; Javed, T.; Ghaffari, A. Heat transfer in MHD stagnation point flow of a ferrofluid over a stretchable rotating disk. *J. Mol. Liq.* **2016**, *219*, 526–532. [[CrossRef](#)]
20. Prabhakar, B.; Bandari, S.; Kumar, K. MHD stagnation point flow of a casson nanofluid towards a radially stretching disk with convective boundary condition in the presence of heat source/sink. *J. Nanofluids* **2016**, *5*, 679–686. [[CrossRef](#)]
21. Ahmed, A.; Khan, M.; Ahmed, J.; Hafeez, A.; Iqbal, Z. Unsteady stagnation point flow of maxwell nanofluid over stretching disk with joule heating. *Arab. J. Sci. Eng.* **2020**, *45*, 5529–5540. [[CrossRef](#)]
22. Hafeez, A.; Khan, M.; Ahmed, J. Stagnation point flow of radiative Oldroyd-B nanofluid over a rotating disk. *Comput. Methods Programs Biomed.* **2020**, *191*, 105342. [[CrossRef](#)]
23. Ahmad, S.; Nadeem, S. Hybridized nanofluid with stagnation point past a rotating disk. *Phys. Scr.* **2020**, *96*, 025214. [[CrossRef](#)]
24. Gowda, R.J.; Rauf, A.; Naveen Kumar, R.; Prasannakumara, B.C.; Shehzad, S.A. Slip flow of Casson–Maxwell nanofluid confined through stretchable disks. *Indian J. Phys.* **2022**, *96*, 2041–2049. [[CrossRef](#)]
25. Rana, P.; Mackolil, J.; Mahanthesh, B.; Muhammad, T. Cattaneo–Christov Theory to model heat flux effect on nanoliquid slip flow over a spinning disk with nanoparticle aggregation and Hall current. *Waves Random Complex Media* **2022**, 1–23. [[CrossRef](#)]
26. Rana, P.; Mahanthesh, B.; Thriveni, K.; Muhammad, T. Significance of aggregation of nanoparticles, activation energy, and Hall current to enhance the heat transfer phenomena in a nanofluid: A sensitivity analysis. *Waves Random Complex Media* **2022**, 1–23. [[CrossRef](#)]
27. Gowda, R.J.; Kumar, R.N.; Rauf, A.; Prasannakumara, B.C.; Shehzad, S.A. Magnetized flow of sutterby nanofluid through cattaneo-christov theory of heat diffusion and stefan blowing condition. *Appl. Nanosci.* **2021**, 1–10. [[CrossRef](#)]
28. Rosseland, S. *Astrophysik und Atom-Theoretische Grundlagen*; Springer: Berlin/Heidelberg, Germany, 1931; pp. 41–44.
29. Viskanta, R.; Grosh, R.J. Boundary layer in thermal radiation absorbing and emitting media. *Int. J. Heat Mass Transf.* **1962**, *5*, 795–806. [[CrossRef](#)]
30. Perdikis, C.; Raptis, A. Heat transfer of a micropolar fluid by the presence of radiation. *Heat Mass Transf.* **1996**, *31*, 381–382. [[CrossRef](#)]
31. Cortell, R. A numerical tackling on Sakiadis flow with thermal radiation. *Chin. Phys. Lett.* **2008**, *25*, 1340. [[CrossRef](#)]
32. Pantokratoras, A. Natural convection along a vertical isothermal plate with linear and non-linear Rosseland thermal radiation. *Int. J. Therm. Sci.* **2014**, *84*, 151–157. [[CrossRef](#)]
33. Mahanthesh, B. Quadratic Radiation and Quadratic Boussinesq Approximation on Hybrid Nanoliquid Flow. In *Mathematical Fluid Mechanics*; De Gruyter: Berlin, Germany, 2021; pp. 13–54.
34. Thriveni, K.; Mahanthesh, B. Significance of variable fluid properties on hybrid nanoliquid flow in a micro-annulus with quadratic convection and quadratic thermal radiation: Response surface methodology. *Int. Commun. Heat Mass Transf.* **2021**, *124*, 105264.
35. Shaw, S.; Samantaray, S.S.; Misra, A.; Nayak, M.K.; Makinde, O.D. Hydromagnetic flow and thermal interpretations of Cross hybrid nanofluid influenced by linear, nonlinear and quadratic thermal radiations for any Prandtl number. *Int. Commun. Heat Mass Transf.* **2022**, *130*, 105816. [[CrossRef](#)]
36. Purna Chandar Rao, D.; Thiagarajan, S.; Srinivasa Kumar, V. Significance of quadratic thermal radiation on the bioconvective flow of Ree-Eyring fluid through an inclined plate with viscous dissipation and chemical reaction: Non-Fourier heat flux model. *Int. J. Ambient. Energy* **2022**, 1–13. [[CrossRef](#)]
37. Rana, P.; Gupta, S.; Gupta, G. Unsteady nonlinear thermal convection flow of MWCNT-MgO/EG hybrid nanofluid in the stagnation-point region of a rotating sphere with quadratic thermal radiation: RSM for optimization. *Int. Commun. Heat Mass Transf.* **2022**, *134*, 106025. [[CrossRef](#)]

38. Reddy, J.N. *An Introduction to the Finite Element Method*; McGraw-Hill: New York, NY, USA, 2004; Volume 1221.
39. Rana, P.; Makkar, V.; Gupta, G. Finite element study of bio-convective Stefan blowing Ag-MgO/water hybrid nanofluid induced by stretching cylinder utilizing non-Fourier and non-Fick's laws. *Nanomater.* **2021**, *11*, 1735.
40. Rana, P.; Shehzad, S.A.; Ambreen, T.; Selim, M.M. Numerical study based on CVFEM for nanofluid radiation and magnetized natural convected heat transportation. *J. Mol. Liq.* **2021**, *334*, 116102. [[CrossRef](#)]
41. Swapna, G.; Kumar, L.; Rana, P.; Kumari, A.; Singh, B. Finite element study of radiative double-diffusive mixed convection magneto-micropolar flow in a porous medium with chemical reaction and convective condition. *Alex. Eng. J.* **2018**, *57*, 107–120. [[CrossRef](#)]
42. Thriveni, K.; Mahanthesh, B. Sensitivity computation of nonlinear convective heat transfer in hybrid nanomaterial between two concentric cylinders with irregular heat sources. *Int. Commun. Heat Mass Transf.* **2021**, *129*, 105677. [[CrossRef](#)]
43. Areekara, S.; Mackolil, J.; Mahanthesh, B.; Mathew, A.; Rana, P. A study on nanoliquid flow with irregular heat source and realistic boundary conditions: A modified Buongiorno model for biomedical applications. *ZAMM-J. Appl. Math. Mech./Z. Für Angew. Math. Und Mech.* **2022**, *102*, e202100167. [[CrossRef](#)]
44. Shevchuk, I.V. *Modelling of Convective Heat and Mass Transfer in Rotating Flows*; Springer International Publishing: Basel, Switzerland, 2016; pp. 1–235.
45. Shevchuk, I.V. *Convective Heat and Mass Transfer in Rotating Disk Systems*; Springer: Berlin/Heidelberg, Germany, 2009; Volume 45.